



Array-source X-ray velocimetry

G. W. GOONAN,^{1,*} A. FOURAS,^{1,2} AND S. DUBSKY¹

¹*Department of Mechanical and Aerospace Engineering, Monash University, Clayton, VIC, 3800, Australia*

²*4Dx Ltd., Melbourne, VIC, 3004, Australia*

*george.goonan@monash.edu

Abstract: X-ray velocimetry (XV) has shown promise for investigations into various dynamic biological systems, including the motion of lungs and the flow of blood. Prior research in the field of XV has highlighted the need for both high spatial resolution to resolve features for tracking, and temporal resolution for accurate velocity measurement. In X-ray imaging systems, enhancement of spatial and temporal resolution requires a small focal spot size and high power output respectively, increasing anode power density requirements. In this paper, we present a multi-source XV regime whereby simultaneously illuminating a sample with multiple sources of small focal spot size, overall illumination can be increased whilst maintaining minimal source blurring without increasing power density requirements. Through a series of simulations, we demonstrate the capability for multi-source systems under various practical constraints, such as focal spot size and power density, to provide increased accuracy compared to single source systems.

© 2018 Optical Society of America under the terms of the [OSA Open Access Publishing Agreement](#)

OCIS codes: (170.7440) X-ray imaging; (120.4570) Optical design of instruments.

References and links

1. A. Fouras, M. J. Kitchen, S. Dubsky, R. A. Lewis, S. B. Hooper, and K. Hourigan, "The past, present, and future of x-ray technology for in vivo imaging of function and form," *J. Appl. Phys.* **105**(102009), 1–14 (2009).
2. Y. Suzuki, N. Yagi, and K. Uesugi, "X-ray refraction-enhanced imaging and a method for phase retrieval for a simple object," *J. Synchrotron Radiat.* **9**(3), 160–165 (2002).
3. A. Fouras, B. J. Allison, M. J. Kitchen, S. Dubsky, J. Nguyen, K. Hourigan, K. K. Siu, R. A. Lewis, M. J. Wallace, S. B. Hooper, M. Wallace, and S. Hooper, "Altered lung motion is a sensitive indicator of regional lung disease," *Ann. Biomed. Eng.* **40**(5), 1160–1169 (2012).
4. S. Dubsky, S. B. Hooper, K. K. Siu, and A. Fouras, "Synchrotron-based dynamic computed tomography of tissue motion for regional lung function measurement," *J. R. Soc. Interface* **9**(74), 2213–2224 (2012).
5. R. A. Jamison, K. K. Siu, S. Dubsky, J. A. Armitage, and A. Fouras, "X-ray Velocimetry within the ex vivo carotid artery," *J. Synchrotron Radiat.* **19**(6), 1050–1055 (2012).
6. R. A. Jamison, S. Dubsky, K. K. Siu, K. Hourigan, and A. Fouras, "X-ray Velocimetry and haemodynamic forces within a stenosed femoral model at physiological flow rates," *Ann. Biomed. Eng.* **39**(6), 1643–1653 (2011).
7. H. Park, E. Yeom, and S. J. Lee, "X-ray PIV measurement of blood flow in deep vessels of a rat: An in vivo feasibility study," *Sci. Rep.* **6**(1), 19194 (2016).
8. A. S. Schlachter, "Third-Generation Synchrotron Light Sources," in *NATO Advanced Study Institute on New Directions in Research with Third-Generation Soft X-Ray Synchrotron Radiation Sources* (Maratea, 1992).
9. Z. Huang, "Brightness and Coherence of Synchrotron Radiation and FELs," in *IPAC*, Shanghai, 2013.
10. O. Svelto, *Principles of Lasers* (Springer, 2010).
11. B. Yazıcı, I.-Y. Son, A. Jin, and X. G. Xu, "Applications to Optimization of X-Ray Radiographic Imaging," in *Handbook of Anatomical Models for Radiation Dosimetry* (Taylor and Francis Group, 2010), pp. 525–547.
12. I. Ng, D. M. Paganin, and A. Fouras, "Optimisation of in-line phase contrast particle image velocimetry using a laboratory x-ray source," *J. Appl. Phys.* **112**, 074701 (2012).
13. B. Gonzales, D. Spronk, Y. Cheng, A. W. Tucker, M. Beckman, O. Zhou, and J. Lu, "Rectangular Fixed-Gantry CT Prototype: Combining CNT X-Ray Sources and Accelerated Compressed Sensing-Based Reconstruction," *IEEE Access* **2**, 971–981 (2014).
14. G. Travish, F. J. Rangel, M. A. Evans, B. Hollister, and K. Schmiedehausen, "Addressable flat-panel x-ray sources for medical, security, and industrial applications," in *SPIE*, San Diego, 2012.
15. X. Qian, R. Rajaram, X. Calderon-Colon, G. Yang, T. Phan, D. S. Lulush, J. Lu, and O. Zhou, "Design and characterization of a spatially distributed multibeam field emission x-ray source for stationary digital breast tomosynthesis," *Med. Phys.* **36**(10), 4389–4399 (2009).
16. S. Wang, X. Calderon, R. Peng, E. C. Schreiber, O. Zhou and S. Chang, "A carbon nanotube field emission multi-pixel x-ray array source for microradiotherapy application," *App. Phys. Lett.* **98**, 213701 (2011).

17. R. P. Murrie, D. M. Paganin, A. Fouras, and K. S. Morgan, "Phase Contrast X-Ray Velocimetry of Small Animal Lungs: Optimising Imaging Rates," *Biomed. Opt. Express* **7**(1), 79–92 (2016).
18. J. H. Hubbell and S. M. Seltzer, "Tables of X-ray mass attenuation coefficients and mass energy absorption coefficients from 1 keV to 20 MeV for elements Z=1 to 92 and 48 additional substances of dosimetric interest," National Institute of Standards and Technology, 2011. [Online]. Available: <http://physics.nist.gov/PhysRefData/XrayMassCoef/cover.html>.
19. Q. Xu, *A Handbook of Mouse Models of Cardiovascular Disease* (John Wiley & Sons, 2006).
20. Varian Medical Systems, "PaxScan 2020+," May 2011. [Online]. Available: <https://www.varian.com/media/1826/browser>. [Accessed 28 January 2015].
21. S. C. Irvine, *Studies in X-Ray Dynamic Speckle Imaging* (Melbourne: Doctoral Thesis, Monash University, 2010).
22. T. E. Gureyev, Y. I. Nesterets, A. W. Stevenson, P. R. Miller, A. Pogany, and S. W. Wilkins, "Some simple rules for contrast, signal-to-noise and resolution in in-line x-ray phase-contrast imaging," *Opt. Express* **16**(5), 3223–3241 (2008).
23. D. L. Davies and D. W. Bouldin, "A Cluster Separation Measure," *IEEE Trans. Pattern Anal. Mach. Intell.* **1**(2), 224–227 (1979).
24. A. Fouras and J. Soria, "Accuracy of out-of-plane vorticity measurements derived from in-plane velocity field data," *Exp. Fluids* **25**(5-6), 409–430 (1998).

1. Introduction

In both scientific research and medical practice, the vast majority of biological systems investigated are dynamic in nature. The development of suitable high spatio-temporal resolution dynamic imaging systems is therefore critical in order to observe and analyze these processes in motion. A number of methodologies including ultrasound, magnetic resonance imaging (MRI), positron emission tomography (PET) and X-ray Velocimetry (XV) have been developed in response to the growing requirement for the investigation of motion and flow in biological systems [1]. Amongst these technologies, x-ray based methods have been shown to provide the highest possible resolutions, whilst additionally being affordable and widely available. Materials with a low x-ray absorption-contrast can be imaged by utilizing Phase Contrast Imaging (PCI) techniques, further increasing the breadth of potential XV applications [2]. The velocity fields resulting from XV can be further processed to yield other important physiological properties, such as the expansion of lung tissue [3, 4] and shear stress in blood flow [5, 6].

XV techniques, however, are not without their shortfalls. Indeed, the required power of an x-ray source to achieve appropriate temporal resolutions for *in vivo* analysis has proven to be exceptionally prohibitive throughout the biological sciences [7]. Though recent technological innovation has led to third generation synchrotron [8] and fourth generation X-ray Free Electron Laser (XFEL) sources [9] with excellent power densities and coherence capable of *in vivo* analysis, such technologies can boast neither the availability nor the affordability of simpler conventional x-ray sources. This has led to a divide between the depth of analytical techniques available to scientific research and the relative lack thereof in small animal research laboratories and medical practice. The aforementioned properties of coherence and power density are only two of those to be considered when designing and utilising an x-ray source; Monochromaticity, directionality, exposure time and focal spot size are equally important factors to consider [10]. Whilst the desired optimisation of many of these parameters can be straightforward, great care must be taken balancing source optimisation with radiation dose when developing systems for medical applications [11]. Moreover, it has been shown that optimisation for Particle Image Velocimetry (PIV) analysis requires simultaneous balancing of the above parameters and further parameters such as geometric magnification and pixel size [12], adding an additional layer of complexity to the design of PCI-based XV systems.

In this paper we conceptualize a multi-source XV regime utilizing array source technology, demonstrating the potential of such a regime to increase the accuracy of XV analysis with reduced power density requirements via judicious selection of source location and system geometry. This is completed via a series of numerical simulations of mouse lung tissue, and consequently analysing the accuracy of PIV analysis when imaging using single

source and multi-source systems. We begin by outlining some background information regarding the technology investigated throughout this paper, including array sources (§2.1) and XV analysis (§2.2). We follow by detailing the method used in this paper to simulate a given biological system (§3.1 through to §3.3), and a brief discussion regarding the critical factors explored throughout this paper (§3.4 and §3.5). The results of the initial investigation into multi-source system performance is then examined in §4.1. Using these results, we detail a method by which a given system can be optimised for XV analysis with array source technology, and demonstrate its superior performance to traditional single source systems (§4.2). We conclude with a brief discussion on a number of points raised throughout this paper (§5).

2. Background

2.1 Array source technology

With the introduction of x-ray array source technology [13, 14], further varieties of imaging methods have been made possible, such as stationary digital breast tomosynthesis [15] and micro-beam radiation therapy [16]. These sources consist of multiple individual sources, often constructed from carbon nanotubes, arranged in an array or array-like structure. Of particular interest to this project are addressable array sources, wherein individual sources may be switched on or off at the user's command [14]. Such sources, in addition to the above properties of lateral scanning without source movement and increased configurability compared to usage of apertures, demonstrate inherent source redundancy that can lead to a longer product life cycle. A visualization of such technology in this paper's proposed method of usage, along with a comparison to traditional single source systems can be seen in Fig. 1. Here, a single source with high power density creates a sharp image. As the power density of the source decreases, the spot size is increased to counteract the loss of brightness, at the cost of blurring. Alternatively, multiple sources project a single object to the detector, and this new combined 'feature' can then be tracked using PIV techniques, whilst maintaining image sharpness and increasing the overall system flux.

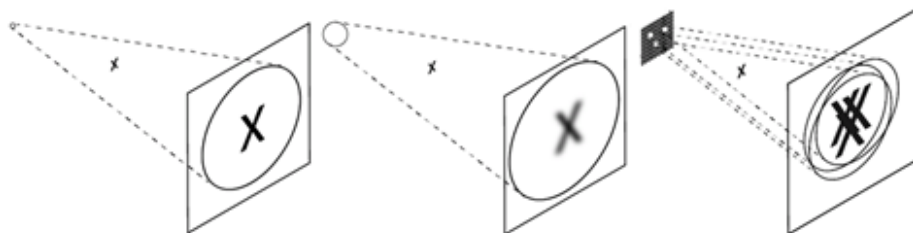


Fig. 1. Visualization of various source technologies. Left: A small spot size with a suitably high power density produces a sharp image. Center: As power density decreases, a source's spot size may be increased to counteract the loss of brightness, at the cost of blurring. Right: An array source maintains the sharpness of a small spot size, whilst generating multiple images of the same object.

2.2 XV analysis

X-ray Velocimetry describes the method of using x-ray imaging apparatus in conjunction with Particle Image Velocimetry (PIV) techniques, wherein the cross-correlation of x-ray images at two different time points is used to calculate the displacement (and hence equivalently, the velocity) of particles present in both images. These particles need not necessarily be distinct, but rather a recognizable feature or pattern that can be observed changing position over time, as is the case for objects that produce images such as the speckle patterns resulting from lung alveoli in chest x-rays as shown in Fig. 2. In such systems, PIV recognizes a speckle pattern created by a cluster of alveolar structures, and correlates the location of this cluster from one image to the next.

Analysis is performed within interrogation regions across the generated images, giving a vector for each region based on the position of the maximum correlation. For computational efficiency, it is generally accepted that particles in a region will travel no further than half the width of one window per frame. This in turn becomes a constraint on the imaging system, such that the image exposure and capture rate must be fast enough to ensure that particle displacements remain below this limit.

As shown in Fig. 1, a multi-source imaging system can maintain the sharpness of the multiple images produced, whilst increasing overall flux. Each image will displace proportionally with the sample displacement, and hence the maximum correlation produced in the XV analysis will still be representative of the underlying sample displacement, despite the multiple images. We propose, therefore, that increasing overall flux by adding multiple small sources, thus maintaining image sharpness, will result in improved accuracy and temporal resolution as compared to increasing the single source size.

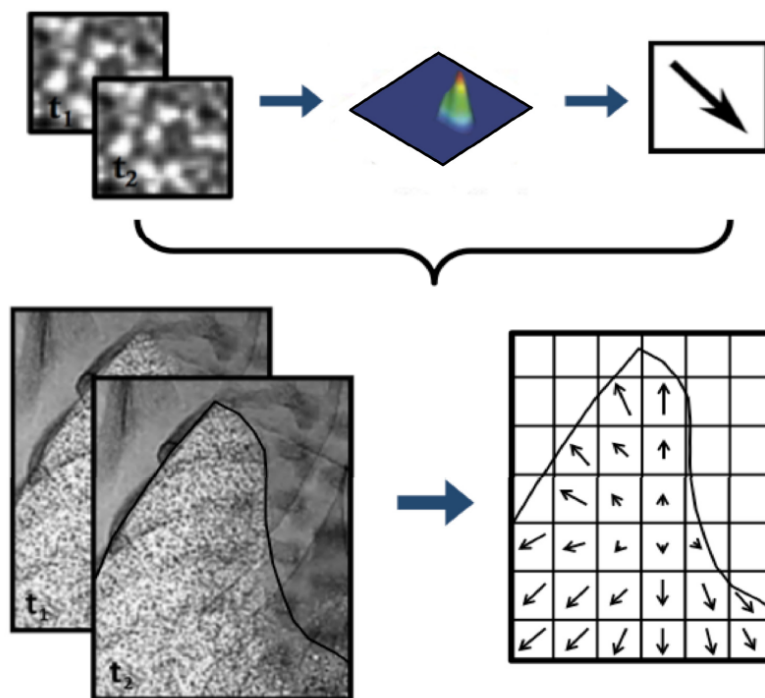


Fig. 2. An example of the XV process. Two images at two different time points are taken, and the cross-correlation of each window is calculated. The peak of this cross-correlation determines the displacement, and hence velocity, of the feature identified in each window.

3. Methodology

In order to assess the improvements in accuracy and resolution that can be achieved using array-source x-ray systems, we conducted a parametric study via numerical simulation methods. In this study, we simulate alveolar clusters in mice, using the parameters observed on Monash University's liquid metal jet X-ray system, and further system variations derived from these parameters. After generation of an image-pair formed from a seeded volume under flow, we assess the relative accuracy of PIV analysis for each system.

3.1 Synthetic phantom generation

Following the method as set out by Murrie *et. al.* [17], alveolar clusters are constructed as a 200 μm cavity of air inside a sphere of mouse lung tissue with a complex refractive index of n

$= 1 - \delta + i\beta$ ($\delta = 4.15 \times 10^{-7}$, $\beta = 2.42 \times 10^{-10}$ [18]), and simulated using the wave spectrum and geometric properties of source to object distance r_1 (333 mm), and object to detector distance r_2 (3025 mm), as observed on Monash University's liquid metal jet x-ray system (MetalJet D2, Excillum, Sweden). The result of this process is a single high-resolution phase contrast image of a single particle as would be seen by a flawless detector when projected by a source with infinite power density. The images of particles generated at this stage are of 100x finer resolution than the detector they will be projected onto, in order to ensure the accuracy of images generated from the phantom. A volume is then seeded at a given particle seeding density with the above particles. In order to approximate the effects of surrounding tissue on the resultant image, an approximation of the flat-body attenuation caused by the average mouse chest thickness is added to the phantom, calculated by multiplying the average thickness of 1.5cm [19] by the mass attenuation coefficient of soft tissue as found in the NIST Tables [18].

3.2 Imaging system

With the synthetic phantom complete, the remainder of the imaging system is modelled, involving the selection of a source, detector, scintillator, and fixation of the phantom in 3D space. As the detector and scintillator chosen will remain constant throughout all simulations conducted, we use the PaxScan 2020 + [20] with in-built integral columnar CsI:Ti scintillator currently used in conjunction with the Excillum system as described above. The location of the phantom is fixed using the parameters r_1 and r_2 as provided during phantom generation, and such that the centre of the region of interest under observation is located between the centre of the source or source array and the centre of the detector. A visual representation of the above system is shown in Fig. 3. The simulated source used, as the primary parameter under investigation, varies from simulation to simulation. For multi-source systems, the source array used follows the general design of an addressable array source as seen in Travish *et. al.* [14], with variations in source size, separation and power density.

With the above physical parameters set, each particle within the phantom is projected by the source(s) onto the detector. This is completed via a combination of ray tracing and rastering techniques, wherein the high resolution phase contrast images previously generated for the particles present in the volume are traced from the object plane to the detector plane, binned into their respective detector pixels, and summed across all projections of particles produced by each source. A similar model of projection, from which the implemented model is based, can be found in Irvine [21]. Following the guidelines as set out by Gureyev *et. al.* [22], we then apply source and scintillator blurring to the image according to the respective selections made when modelling the imaging system. Next, motion blur is applied using the appropriate convolution kernel as dictated by the flow under observation. Finally, source and detector noise & efficiency are simulated via photon statistics, the values for which are determined by using the physical product specifications of the devices described above, in conjunction with experimentally validated measurements of background noise and detector throughput, scaled to the parameters of the simulated source and detector in use. An example of the complete system simulated throughout this project can be seen in Fig. 3, with an accompanying example of a single particle's projection in Fig. 4.

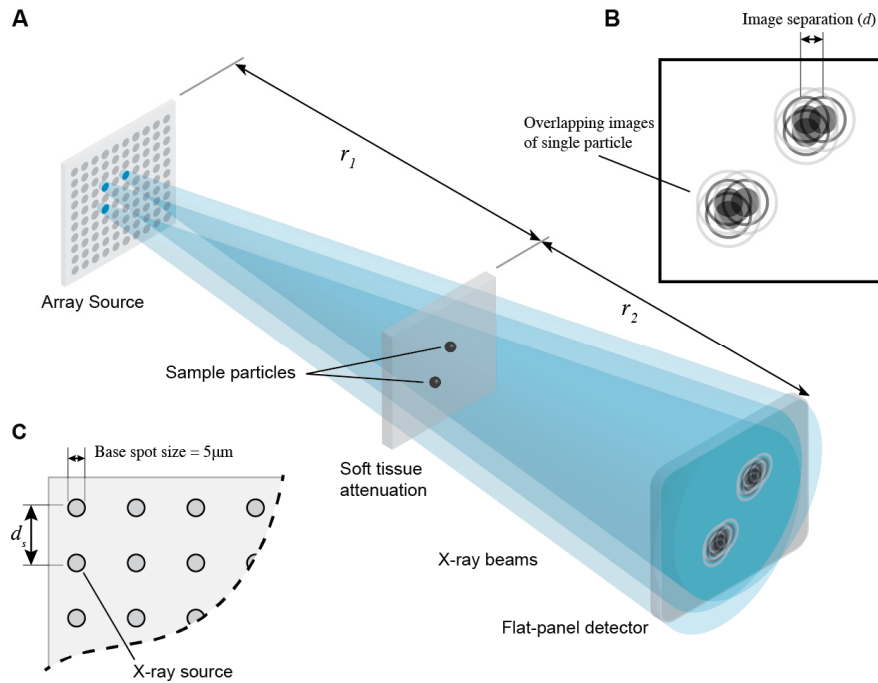


Fig. 3. An example of the system simulated in this paper. Each of the variables in this system, including all source and detector properties, are digitally reproduced in order to provide simulations of the highest possible accuracy.

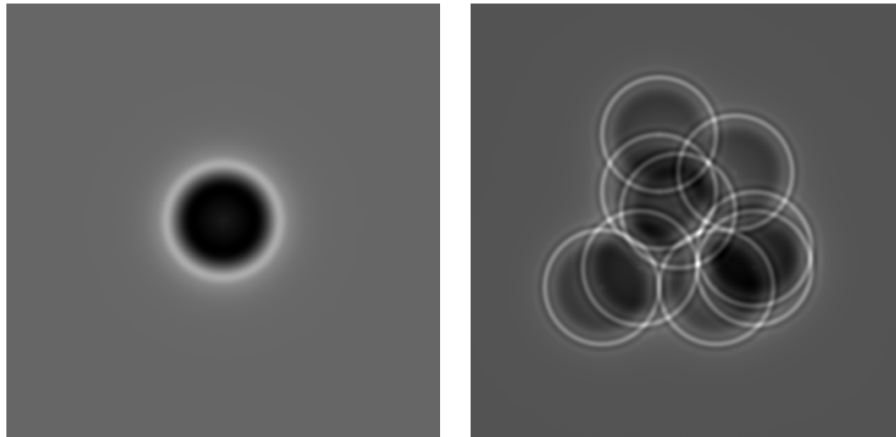


Fig. 4. Example images of a projection of a single particle by a multi-source system (right) consisting of 9 $5\mu\text{m}$ sources, and the equivalent single source system (left) consisting of a $15\mu\text{m}$ source. The resolution on these images has been enhanced by a factor of 10, in order to allow for easier visual identification of differences by the reader, such as sharpness and constructive/destructive interference. In particular, the loss of phase contrast rings as spot size increases can be clearly observed, owing to an increase in penumbral blur.

3.3 PIV analysis

To assess the relative accuracy of each method, a homogeneous shear flow with a linear velocity profile, minimum displacement of zero and maximal displacement of 10 mm/s is applied to the phantom, giving an interframe displacement of approximately 36 px/frame. Multi-pass PIV was performed with an initial window size of 128 px to ensure adequate

capture of flow dynamics, with subsequent passes of 64 px and 32 px in order to test PIV accuracy at higher spatial resolutions. In order to evaluate the accuracy of the PIV analysis, the results calculated are compared to the known input displacement. By subtracting the known displacement from the calculated displacement for each individual window observed, a matrix of error values is generated. The mean and standard deviation of these error values can then be used to determine the average accuracy of the calculated displacement, the extent of bias errors, and the variation in error caused by variation in parameters. These evaluations are conducted across numerous system designs to generate a sample space mapping.

3.4 Parametric study

In order to reduce computation time and the length of the investigation to a practical level, it is necessary to consider which factors are most critical to investigate. First and foremost, this investigation looks to develop a regime or system design suitable for medical applications. It is therefore critical to ensure that dose efficiency be maximized, or equivalently, that the intensity incident on a body be minimized. In this regard, we will consider three factors that have significant impact on incident intensity: exposure time (1-30 ms), focal spot size (5-31.6 μm), and power density (125-3000 kW/mm^2). To note, these power densities approximately represent a range from a stationary tungsten anode, through to a liquid metal-jet anode. Additionally, with respect to power density, the focus of this study is to provide insight into potential multi-source systems that are accessible to small-animal research or medical imaging suites. It is hence at these lower power densities that our investigation will focus its attention. Further details on this matter are explored in §5. Discussion.

Using the above parameters as domains, a preliminary sample space of PIV error across 51 exposure times, 37 focal spot sizes (and equivalently for multi-source systems, number of sources), and 11 power densities was constructed, in order to observe the effect of variation of these three parameters on the PIV error. For each of these points, 20 unique source configurations were evaluated for multi-source systems, and 10 unique particle seedings were evaluated for single source systems, giving a total of 622,710 images each containing 931 PIV windows used to generate the sample space.

3.5 Configuration dependency

With respect to multi-source systems, the results observed for a given set of system parameters will have a dependence on the spatial configuration of its sources. It is hence desirable to analyze not only the comparison between single source and multi-source systems, but also the relationship between multi-source systems of differing configurations. To this end, each of the 20 source configurations used were randomized in order to provide an unbiased observation of the complete distribution of source configurations. In addition, these configurations were tested at numerous source separation scales, in order to observe the effects of source clustering. This selection of configurations, although only a small portion of the complete set of configurations (e.g. 20 configurations of 10 sources selected from a 10×10 grid = $3.18 \times 10^{-17}\%$ of the complete distribution), when combined with the 20,757 points that constitute the preliminary sample space, provide enough information to make informed observations regarding configurations and their general effect on PIV analysis.

4. Results

Two aspects of multi-source system performance were explored in this study. The effect of the multi-source configuration parameters of source separation and source placement on image quality and PIV error was analysed, in order to understand how different multi-source systems perform. Subsequently, the performance of multi-source systems was compared to single source systems to understand the potential benefits that may be achieved. The results displayed here will be examined in depth in the proceeding section.

4.1 Multi-source system analysis

With the accuracy of multi-source systems known to be dependent on source configuration, we began by developing a metric derived from the interaction between two images of one spherical particle formed by two sources. For a given fractional crossover of two circular images n , and assuming that each spherical particle produces an approximately circular image at the detector, we have:

$$d = 2Mr_p \cos(\theta), \text{ where } 2\theta - \sin(2\theta) = n\pi, 0 \leq n \leq 1 \quad (1)$$

where d denotes the separation between the centre of two image circles, M is the geometric magnification, and r_p is the particle radius. The value for θ derived from the analogue to Kepler's equation shown above must be calculated via numerical methods. By considering the geometry involved in projecting a single particle from two sources to produce two images of the particle at a detector, it then follows that the maximum separation between two sources (d_s) such that Eq. (1) is satisfied (ie. that the two images overlap) is:

$$d_s = \frac{2Mr_p \cos(\theta)}{M-1} \quad (2)$$

It can be seen from this equation that the limiting separation scales linearly with the particle radius, and exponentially with magnification. That is, as the geometric magnification approaches unity, the maximum source separation approaches infinity. Conversely, as geometric magnification approaches infinity, the maximum source separation approaches $2r_p \cos(\theta)$.

Taking inspiration from the Davies-Bouldin Index's intra-cluster measure of scatter [23], and building on concepts established from the above equations, we derive the following Clustering Coefficient:

$$C = \frac{1}{\sum_{i=1}^N k_i} * \sum_{i=1}^N \sum_{j=1}^{k_i} \frac{1}{d_{ij}}, \text{ where } d_{ij} = |x_i - x_j|_2, \quad (3)$$

$$k_i = \text{number of sources s.t. } d_{ij} \leq \frac{2Mr_p \cos(\theta)}{M-1}, \text{ and } 2\theta - \sin(2\theta) = n\pi$$

Here, N is the total number of sources, and x_i is the location of source i . The clustering coefficient is a measure of the compactness of a given configuration of sources. For the purpose of Eq. (3) as used in calculating the clustering coefficient, n represents the minimum fractional crossover for which 2 sources are considered to be clustered together. For the simulations conducted, a limiting fractional crossover of $n = 0.25$ was used. It has been observed that this $n = 0.25$ provides a stronger correlation than that of the simple Euclidean distance across all source pairs (i.e. where $n = 0$). A proposed explanation for this is due to the increase in contrast (and hence, signal-to-noise ratio) produced by image overlaps closer to the particle image centre.

A linear relationship between the cluster coefficient and contrast ratio can be seen in Fig. 5, demonstrating improved contrast with greater clustering. This figure also provides a comparison between effects observed in speckle and non-speckle regimes, and demonstrates that the relationship between cluster coefficient and contrast ratio is independent of the presence (or lack therein) of speckle. An inverse relationship between contrast ratio and Standard Deviation (SD) PIV error is shown in Fig. 6, that is, a reduction in error for higher contrast ratios. Here, we define the contrast ratio as the standard deviation of the image intensity values over its mean. Due to identical photon counts for our simulations, this is simplified to the standard deviation in Fig. 5. & 6. for the purpose of readability. Finally, in Fig. 6., we observe three modes across three source separations. For small source separations, there is a strong correlation between contrast ratio (and hence cluster coefficient) and SD PIV

error. As this source separation increases, the range of contrast ratios decreases, relating to the inability to cluster sources. Finally, at large separations, there is a shift in regime when clustering becomes impossible, and the relationship found in smaller source separations no longer holds.

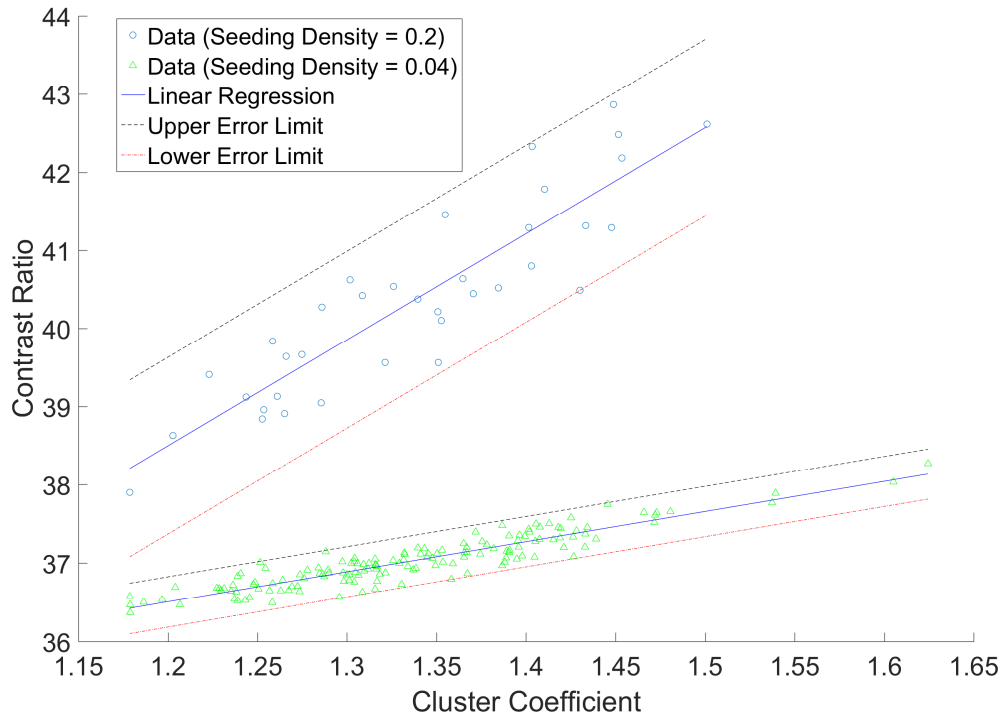


Fig. 5. Contrast Ratio vs. Cluster Coefficient for an inter-source separation of $20\ \mu\text{m}$ ($r_p/10$) at two different particle seeding densities. In the higher seeding density, individual particles are indistinguishable from one another, and a speckle regime is present. This is in contrast to the lower seeding density, where individual particles can still be identified. For both data sets, the coefficient of determination, $r^2 > 0.95$.

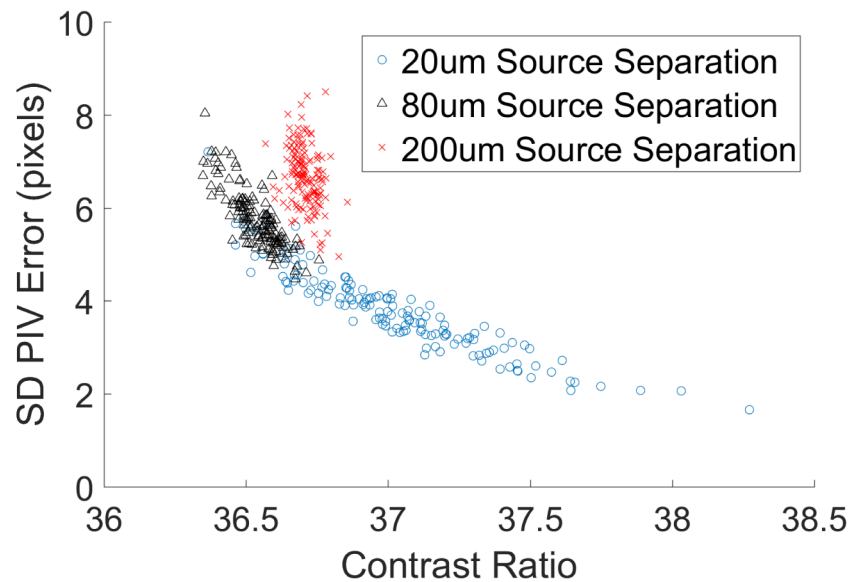


Fig. 6. Contrast Ratio vs. SD PIV Error. Three main modes can be observed in the data presented. For small source separations, there is a strong correlation between contrast ratio (and hence cluster coefficient) and PIV Error. As this source separation increases, the range of contrast ratios decreases, relating to the inability to efficiently cluster sources. Finally, at large separations, there is a shift in regime when clustering becomes impossible, and the relationship found in smaller source separations no longer holds.

4.2 Single source vs. multi-source: performance evaluation

Contour plots of mean and SD PIV error for varying exposure times and number of sources/source sizes can be seen in Fig. 7 (single source) and Fig. 8 (multi-source). For multi-source systems, sources are configured such as to maximize the clustering coefficient. A fixed power density approximately equivalent to a static tungsten anode (approx. 125 kW/mm^2) with a base spot size of $5 \text{ }\mu\text{m}$ was used. It is clear from these contour plots that the general trends and behaviors of each class of system differ significantly, leading to a distinct difference in optimum configurations. In particular, it can be seen that multi-source systems exhibit peaks and troughs in performance at distinctive intervals of source counts. This is believed to be due to the inherent directionality of source configurations on grid-like arrays for a given number of sources and their consequent interplay with velocity gradients in the observed phantom.

The optimum single source configuration for the given power density is found at an exposure time of 18 ms, and a spot size 1.414 times the base $5 \text{ }\mu\text{m}$ size (i.e. $7.07 \text{ }\mu\text{m}$), with an RMS PIV error of 0.267 px. The optimum multi-source system is found to have an exposure time of 7 ms and 10 sources, with an RMS PIV error of 0.191 px. These values equate to a 29% reduction in error, whilst simultaneously reducing the exposure time (and hence equivalently, improving the temporal resolution) by a factor of 2.6. As the error profile across these regions of minimisation is dominated by SD, the following figures will focus on SD error for the purpose of readability.

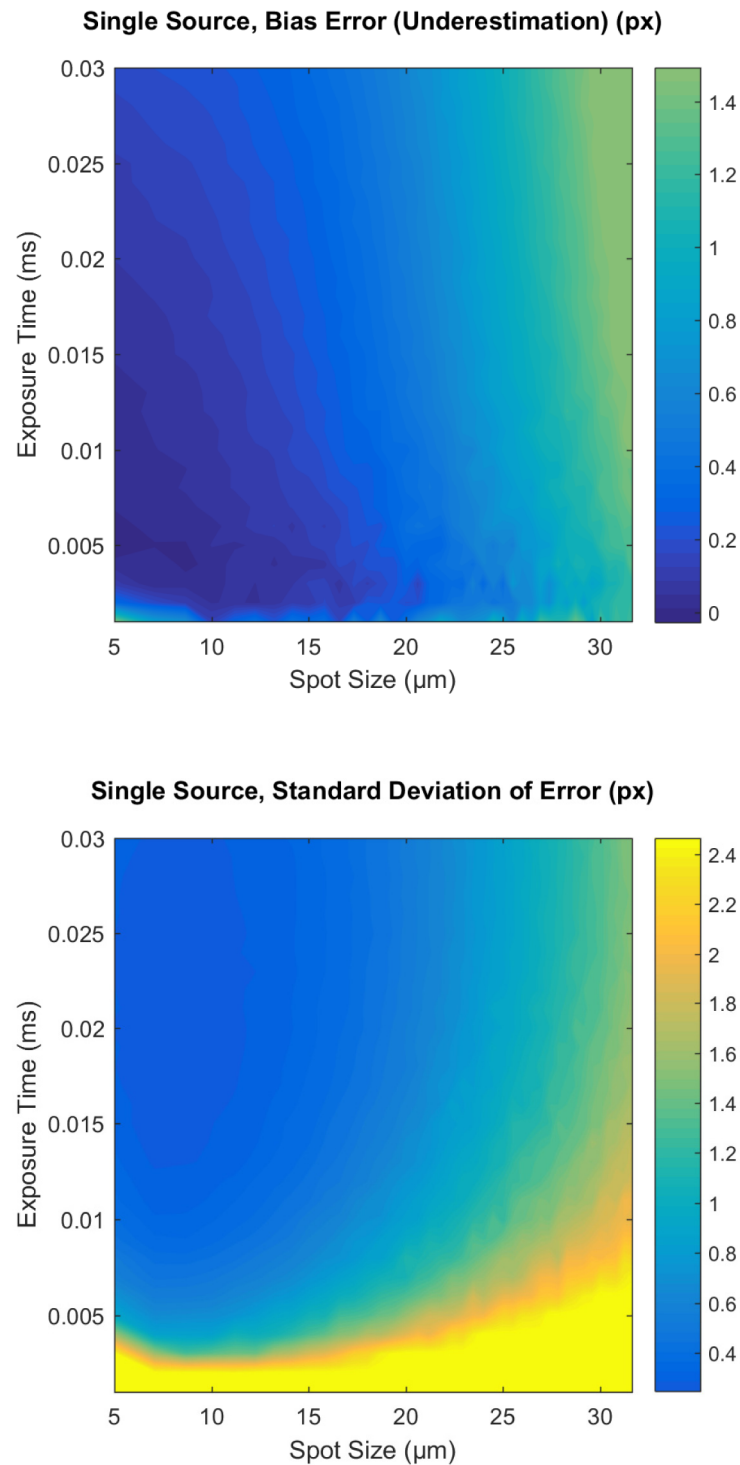


Fig. 7. Source size & exposure time vs. Mean and SD PIV error for a fixed power density single source system with a base focal spot size of 5 μm . An optimum system for the given power density is identified as having a focal spot size of 7.07 μm exposing for 18 ms, with an RMS error of 0.267 px. Regions with an SD error of 2.5 px or greater, or a mean error of 1.5 px or greater, have been capped at 2.5 px and 1.5 px respectively for visibility.

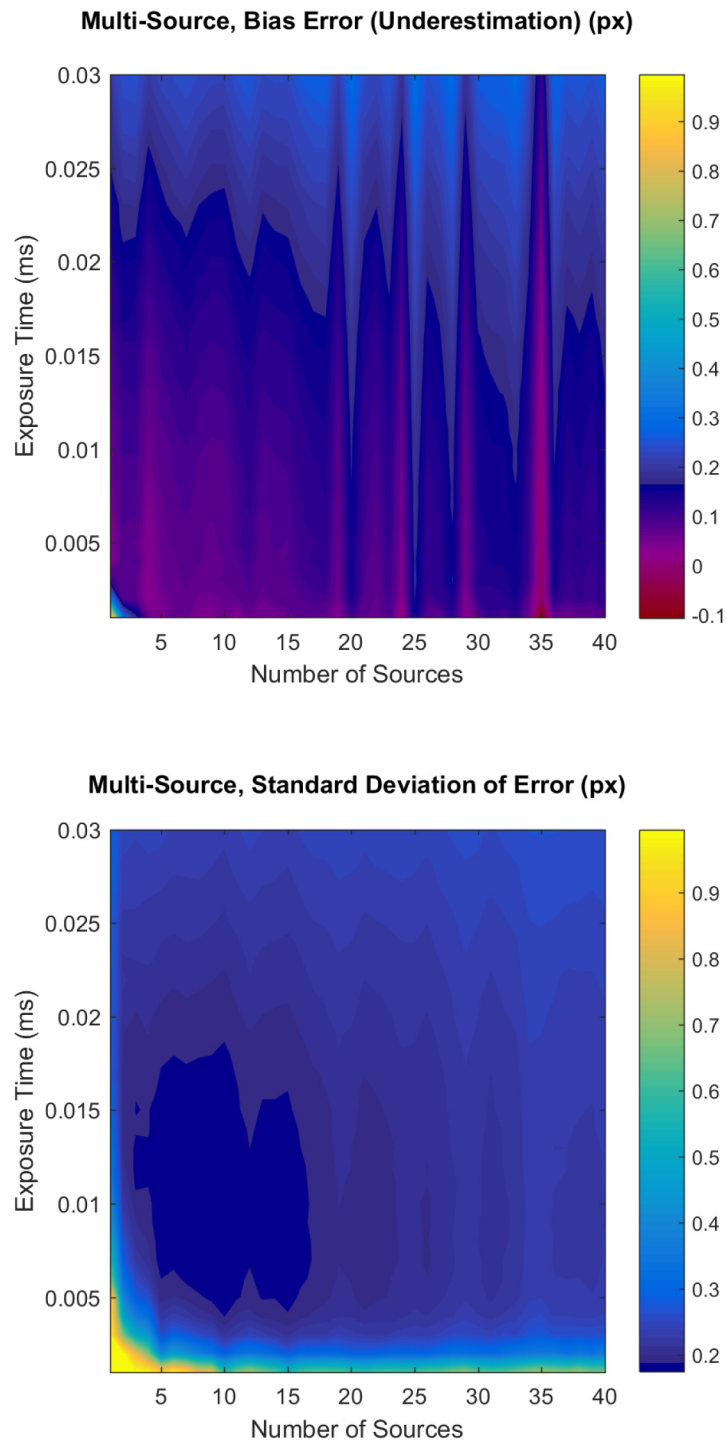


Fig. 8. Number of sources & exposure time vs. Mean and SD PIV error for a fixed power density multi-source system with a focal spot size of $5\ \mu\text{m}$ and source separation of $20\ \mu\text{m}$. Sources are configured such as to maximize the clustering coefficient. An optimum system for the given power density is identified as having 10 sources exposing for 7 ms, with an RMS error of 0.191 px. Regions with an error of 1 px or greater have been capped at 1 px for visibility.

Figure 9 compares the SD PIV error for varying exposure times and source size/number of sources for single source and multi-source systems. Here we see that error increases more rapidly in the single source regime with increasing photon/s, due to increasing penumbral blur not present in the multi-source regime. Additionally, image saturation is present in the high power density systems when exposing for extended periods, seen as a rapid increase in error in both regimes. The SD PIV errors resulting from the optimum source size and number of sources for each exposure time is shown in Fig. 10.

For a given exposure time at low power densities, the accuracy of multi-source systems is significantly higher than the equivalent single source system. For example, in Fig. 9., it can be seen that a low power density multi-source system imaging with 1 ms exposure times demonstrates up to an order of magnitude higher accuracy than any single source system at the same exposure time and power density. In addition, it can be seen that for this particular power density and base spot size, multi-source regimes maintained sub-pixel accuracy at 1 ms of exposure time, whereas single-source regimes failed at exposure times less than 5 ms. Finally, it can be seen that a low power density multi-source system at a given fixed exposure time can provide a comparable accuracy to a higher power density single source system with an identical exposure time.

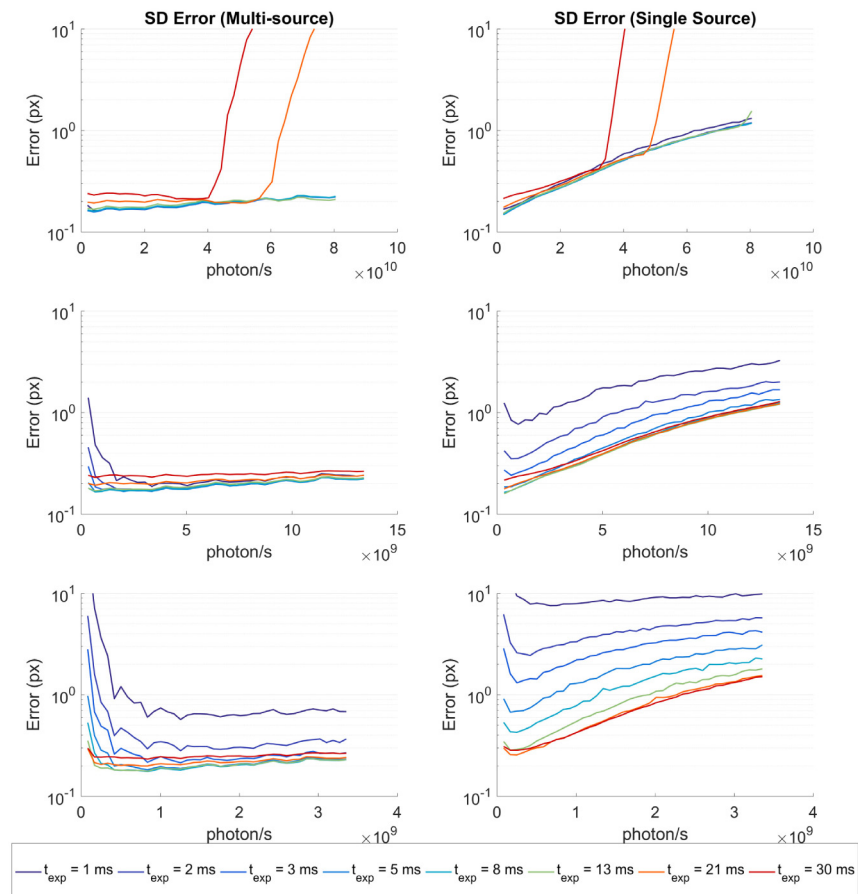


Fig. 9. Multi-source SD error vs. increasing number of sources, and single source SD error vs. increasing spot size, for a given fixed power density. The scale for each plot has been converted into photon/s, for easier comparison. These plots, from top to bottom, represent fixed power densities of 3000 kW/mm², 500 kW/mm², and 125 kW/mm², respectively. SD error has been limited to 10 px, in order to improve visibility. The legend is consistent across all plots.

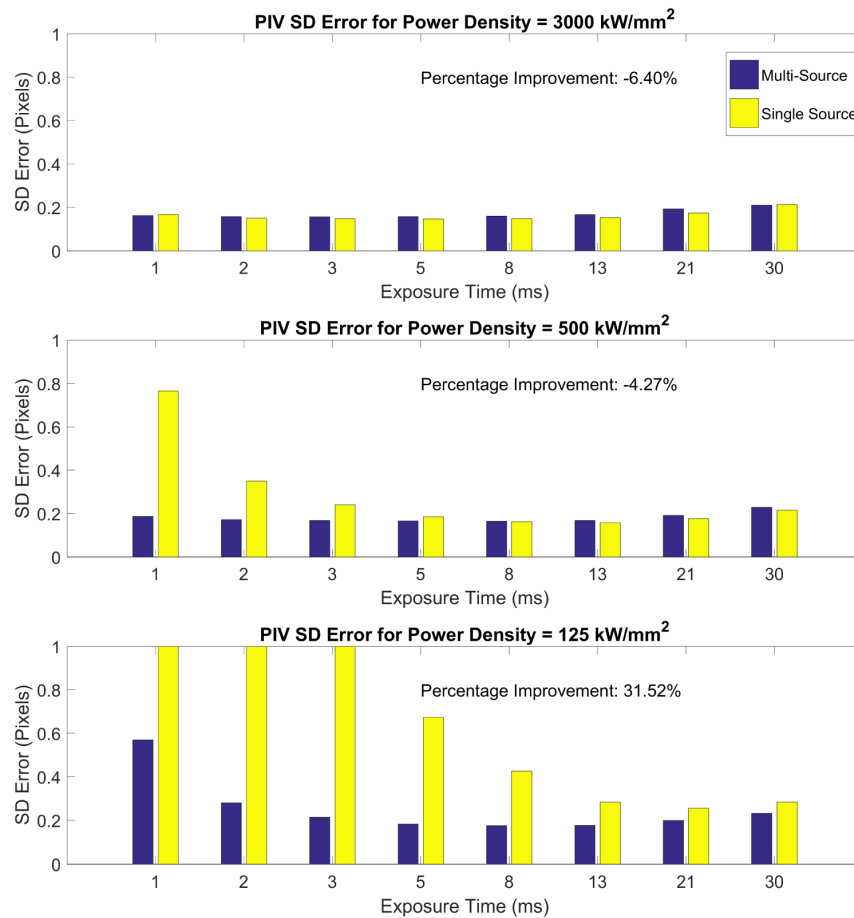


Fig. 10. Comparison of SD error for 125 kW/mm², 500 kW/mm², and 3000 kW/mm². The percentage improvement here represents the reduction in SD error achieved by using the optimum multi-source system as opposed to the optimum single source system, and hence a negative value indicates that the optimal multi-source system results in higher error than the optimum single source system. SD error has been limited to 1 px for visibility. The legend is consistent across all plots.

5. Discussion

The results shown in §4.2 demonstrate that the absolute minimum error of a low power density XV system may be reduced by up to 29% (from 0.267 px to 0.191 px in the above simulations) by using a multi-source system. This in turn demonstrates that for XV system designs that are limited by power density, it would be beneficial to make use of a multi-source design in order to further increase accuracy of results. In addition, it was shown that for a fixed exposure time, multi-source systems could reduce the RMS error of an XV system by up to an order of magnitude when compared to a traditional single source system. Thus we may also conclude that for subjects with high velocity profiles, further benefits may be found by using a multi-source system in order to reduce required exposure times. This is directly equivalent to an increase in the potential temporal resolution of a given system. As the exposure time is increased, multi-source systems approach an error floor faster than single source systems, and hence the disparity between their relative accuracies decreases.

In addition, as a direct consequence of their improved accuracy, multi-source systems present a potential for reduced patient dosage. For example, we may consider the global optimum single source system, with 0.267 px error, as our benchmark selection criteria. This

restricts us to a range of multi-source systems that have equivalent or better accuracy. From this range, we can select a system that has the absolute minimum dosage, or we may further specify other criteria, such as minimisation of exposure time for increased temporal resolution. As a potential candidate, we may decide to make use of a system that has 5 sources exposing for 5ms, which has an RMS error of 0.209 px, along with a reduced dosage per image and increased temporal resolution. This system, in fact, whilst requiring 69.4% of the dosage of the single source global optimum system, simultaneously reduces error by over 20%, and reduces the required exposure time by a factor of 3.6, providing improvements in accuracy, dose and temporal resolution.

To reiterate an above point, a single source system with an infinite power density source would find no benefit from introducing additional sources. Therefore, and as seen in Fig. 10., at a sufficiently high power density the reduction in RMS error is no longer present. The particular critical power density at which this occurs is dependent on numerous parameters such as particle seeding density, velocity profile, and the effect of any additional processing enhancements. For example, when comparing the error values as shown in Fig. 10., we see that by increasing the power density of the system from 125 kW/mm^2 to 500 kW/mm^2 , it is possible for a single source system to out-perform, in terms of the global minimum RMS error, any given multi-source system. The exact point at which the performance of single source systems begins to overtake that of multi-source systems in terms of accuracy must then lie between the two power densities used. For the given system used, this point lies within the range of $400\text{-}500 \text{ kW/mm}^2$, equivalent to a expensive and specialized high power density rotating anode sources. This demonstrates the benefit of multi-source systems across a wide range of typically available X-ray source power densities for the system modelled here (ie. small animal lung imaging). As stated previously, this critical point will of course vary depending on system parameters such as sample, spot size, velocity profile, and so on.

The optimum exposure time is shorter for multi-source systems when compared to single source for a given power density, most clearly shown in Fig. 10. Therefore, for moderate power densities where equivalent accuracy is possible using a single source system, there is still benefit to use of a multi-source system in terms of improved temporal resolution. This is important for fast moving samples, where high temporal resolutions are required to capture the dynamics of the system.

As presented in §4.1, we have developed a metric by which we may approximate the potential benefit found in a particular multi-source system by calculating its Clustering Coefficient. This coefficient suggests that the performance of a multi-source system increases proportionally with the compactness of its configuration. It follows that alterations to source configurations that increase this compactness will lead to improved results. A possible alternative configuration that could achieve this would be a hexagonal close-packed source arrangement, in contrast to a rectangular grid. The potential to develop such a configuration will ultimately depend on additional design factors such as material processing techniques and thermal regulation.

From the results presented in §4.2, we observe the potential for improvement in PIV accuracy and temporal resolution in XV systems by using multi-source systems. As presented previously, common applications for XV include calculations of expansion of lung tissue and shear stress in blood flow, which requires differentiation of the velocity field. It has been shown in previous research that PIV analysis involving expansion, contraction, shear and rotation requires highly accurate displacement estimations in order to reduce the concurrent error in spatial derivatives to acceptable levels [24]. For example, as a vorticity estimate error grows in proportion to the square of the displacement errors, a 29% reduction in PIV error (as seen in this paper) corresponds to 49% less error in the resultant vorticity estimate, a significant improvement in accuracy.

6. Conclusions

We have presented an improved imaging regime for X-ray velocimetry that utilizes multiple sources to maintain sharpness whilst increasing flux. A metric for evaluating the effectiveness of a given multi-source configuration was shown, which demonstrates that performance is highest under a tightly clustering regime. Using this metric, it has been demonstrated that multi-source systems, under compact clustering regimes, exhibit increased accuracy and temporal resolution. It was found that for a low power density system of approximately 125 kW/mm^2 with a base spot size of $5 \text{ }\mu\text{m}$, RMS PIV error could be reduced from 0.267 px in the single source regime, to 0.191 px in the multi-source regime. This corresponds to a reduction in error of 29%. It was also demonstrated that for this particular power density and spot size, multi-source regimes maintained sub-pixel accuracy at 1 ms of exposure time, whereas single-source regimes failed at exposure times less than 5 ms. Furthermore, it was shown that low power density multi-source systems can have equivalent or improved performance compared to some higher power density single-source systems.

These results demonstrate the potential for reduced power density requirements, enabling cheaper and more readily accessible imaging systems to be developed by utilizing a multi-source regime. Such developments will greatly impact the capabilities of small animal research laboratories and medical-grade applications aimed towards observing dynamic processes. In particular, such technology could prove critical in future development of a suitable *in vivo* dynamic imaging system for human lungs, a much needed diagnostic tool for the early detection of numerous pulmonary illnesses.

Funding

Australian Research Council (ARC) (DP150102240).

Acknowledgments

We would like to thank Sarah Irvine for her insight and assistance in the theoretical treatment of high resolution phase contrast imaging, and Rhiannon Murrie & Richard Carnibella for their technical assistance in code development and discussions on simulations. This project was supported by the Multi-modal Australian ScienceS Imaging and Visualisation Environment (MASSIVE; www.massive.org.au).